Ultrasound in Med. & Biol., Vol. 43, No. 10, pp. 2256–2268, 2017

0301-5629/$ - see front matter

http://dx.doi.org/10.1016/j.ultrasmedbio.2017.06.019

● *Original Contribution*

REPRODUCIBILITY AND ANGLE INDEPENDENCE OF ELECTROMECHANICAL WAVE IMAGING FOR THE MEASUREMENT OF ELECTROMECHANICAL ACTIVATION DURING SINUS RHYTHM IN HEALTHY HUMANS

LEA MELKI,* ALEXANDRE COSTET,* and ELISA E. KONOFAGOU*†

*Department of Biomedical Engineering, Columbia University, New York, New York, USA; and †Department of Radiology, Columbia University Medical Center, New York, New York, USA

(*Received* 11 *January* 2017; *revised* 13 *May* 2017; *in final form* 19 *June* 2017)

Abstract—Electromechanical wave imaging (EWI) is an ultrasound-based technique that can non-invasively map the transmural electromechanical activation in all four cardiac chambers *in vivo*. The objective of this study was to determine the reproducibility and angle independence of EWI for the assessment of electromechanical activation during normal sinus rhythm (NSR) in healthy humans. Acquisitions were performed transthoracically at 2000 frames/s on seven healthy human hearts in parasternal long-axis, apical four- and two-chamber views. EWI data was collected twice successively in each view in all subjects, while four successive acquisitions were obtained in one case. Activation maps were generated and compared (i) within the same acquisition across consecutive cardiac cycles; (ii) within same view across successive acquisitions; and (iii) within equivalent left-ventricular regions across different views. EWI was capable of characterizing electromechanical activation during NSR and of reliably obtaining similar patterns of activation. For consecutive heart cycles, the average 2-D correlation coefficient between the two isochrones across the seven subjects was 0.9893, with a mean average activation time fluctuation in LV wall segments across acquisitions of 6.19%. A mean activation time variability of 12% was obtained across different views with a measurement bias of only 3.2 ms. These findings indicate that EWI can map the electromechanical activation during NSR in human hearts in transthoracic echocardiography *in vivo* and results in reproducible and angle-independent activation maps. (E-mail: ek2191@columbia.edu) © **2017 World Federation for Ultrasound in Medicine & Biology.**

Key Words: **Electromechanical wave imaging, Reproducibility, Angle independence, Electromechanical activation sequence, Echocardiography.**

INTRODUCTION

Cardiac conduction abnormalities and arrhythmias can often lead to stroke, heart failure and sudden cardiac death (Mehra 2007; Mozaffarian et al. 2016; Zipes and Wellens 1998). These diseases remain a major cause of death worldwide. In fact, although the rate of deaths attributable to cardiovascular diseases has decreased by 28.8% in the last decade, cardiovascular diseases still accounted for 30.8% of all deaths in the United States in 2013—approximately one of every three deaths (Mozaffarian et al. 2016; Zoni-Berisso et al. 2014). Yet, despite this health impact and the urgent need for prevention, the imaging techniques currently available clinically for heart activation sequence mapping are invasive, ionizing, time consuming and costly (Knackstedt et al. 2008; Packer 2004).

Mapping the electrical activation of the heart is necessary for the diagnosis and treatment of arrhythmias. Providing physicians with simpler tools that allow early detection of arrhythmias and more prompt and precise treatment would undoubtedly improve treatment outcomes. Our group has developed a direct and non-invasive ultrasound-based technique to study the electromechanical behavior of the heart: electromechanical wave imaging (EWI) (Konofagou et al. 2010). This ultrasound-based modality, capable of mapping the electromechanical activation in all four cardiac chambers *in vivo* (Provost et al. 2011a), is transmural and has a high temporal resolution (0.5–3 ms), a high spatial resolution and real-time feedback capabilities (Provost et al. 2010, 2011b; Wang et al. 2008).

The heart needs to be electrically activated before it can mechanically contract (Glass et al. 1991).

Address correspondence to: Elisa E. Konofagou, Department of Radiology, Columbia University Medical Center, 630 West 168th Street, Physicians & Surgeons 19-418, New York, NY 10032, USA. E-mail: ek2191@columbia.edu

The electromechanical wave (EW) refers to the propagation of the onset of the cardiac contraction in response to electrical activation of the heart. The EW has been found to be highly correlated with the electrical activation sequence in the left ventricle (LV), in both normal and paced canines *in vivo* (Provost et al. 2011a, 2011b). Furthermore, the electromechanical delay is defined as the lag between the depolarization of the cardiomyocytes, that is, the electrical activation, and the onset of their contraction, that is, the electromechanical activation. Typically, this delay is on the order of tens of milliseconds (Bers 2002; Cordeiro et al. 2004; Provost et al. 2011a).

Electromechanical wave imaging has been previously reported in a variety of applications, such as ischemia and infarct assessment in canines, as well as cardiac resynchronization therapy (CRT) in heart failure patients. EWI was found capable of detecting infarcted regions in the canine hearts and monitoring the formation of myocardial infarction over several days (Costet et al. 2017). In addition, EWI not only was successful in distinguishing between healthy and heart failure patients, but was also capable of mapping the electromechanical activation pattern of the ventricles under CRT and differentiating responders from non-responders (Bunting et al. 2017).

In previous studies, EWI was reported to be reproducible in simulations and canine experiments (Provost et al. 2011c), as well as repeatable within the same acquisition across consecutive cardiac cycles in open-chest dogs (Costet et al. 2014). However, reproducibility in closed-chest humans has yet to be investigated. Furthermore, it is critical for clinical applications to reliably measure the activation sequence independently of the imaging view. Our group recently established that EWI is capable not only of properly identifying the origin of activation of focal rhythms, but also of distinguishing between epicardial and endocardial origins in a focal paced canine heart *in vivo* (Costet et al. 2016). These findings result from an open-chest animal model and still require further investigation in a closed chest.

Initial results on premature ventricular contractions (PVCs) and Wolff–Parkinson–White (WPW) syndrome patients have been reported (Costet 2016) for potential applications in radiofrequency (RF) ablation treatment planning (Bunting et al. 2016; Papadacci et al. 2017b). Accordingly, it is essential that the arrhythmic focus or re-entry pathway locations identified with EWI remain consistent, no matter the position and orientation of the ultrasound probe. Current techniques for localizing the accessory pathways in patients with WPW in the clinic mostly rely mostly on 12-lead electrocardiogram (ECG) interpretation, intracardiac electrophysiology and fluoroscopy. Recently, non-invasive approaches without radiation exposure have emerged, such as tissue Doppler imaging (Esmaeilzadeh et al. 2013) and 3-D speckle tracking echocardiography (STE) (Ishizu et al. 2016). However, strain imaging with STE on B-mode images typically operates at lower frame rates and is less accurate than RF-based cross-correlation (Walker and Trahey 1995), whereas pulsed wave (PW) Doppler estimation is known to be angle dependent. Therefore, assessing the angle independence of our technique is not only crucial for accurate diagnosis and treatment planning of arrhythmias such as PVCs, persistent atrial fibrillation or focal tachycardia, but would also prove the advantage of EWI over tissue Doppler-based techniques.

In this study, our aim was to determine the reproducibility and angle independence of EWI for the assessment of electromechanical activation during normal sinus rhythm (NSR) in healthy humans *in vivo*. To achieve this goal, activation maps of five healthy male volunteers were generated and compared (i) within the same acquisition across consecutive cardiac cycles; (ii) within the same standard echocardiographic view across successive acquisitions; and finally, (iii) within equivalent LV regions across different imaging views.

METHODS

Experimental protocol

The human subject study protocol was approved by the institutional review board of Columbia University, and informed consent was obtained before all procedures described herein. While lying down on their left side in the lateral decubitus position, seven healthy male volunteers (aged 23 to 33 y) were imaged by a trained cardiologist with a Vantage 256 system (Verasonics, Redmond, WA, USA).

Ultrasound acquisition for EWI was performed in three standard echocardiographic views: parasternal long-axis and apical four- and two-chamber. A 2.5-MHz phased array probe (P4-2 ATL/Philips, Andover, MA, USA) was used to emit unfocused circular waves (Provost et al. 2011a), and to achieve frame rates high enough for displacement estimation applications, RF channel data were acquired at 2000 fps at a 20-cm depth. The latter were followed by a standard 64-line B-mode anatomic acquisition of 1.5 s at 30 fps and 20-cm depth, which was later used for precise manual myocardium segmentation. We acquired RF frames up to four successive times for each view during sinus rhythm. The consecutive scans were recorded less than a minute apart, and the probe was repositioned on the subject between acquisitions. The processing was later performed on a separate computer in MATLAB (The MathWorks, Natick, MA, USA) using a graphics processing unit (GPU) (Tesla NVIDIA, Santa Clara, CA, USA) and parallel processing.

Simultaneous recording of the electrical activity was performed with three electrodes placed on the subject's chest and connected to an ECG unit (77804 A, HP, Palo

Alto, CA, USA). During processing, the ECG data were retroactively used to temporally align the anatomic B-mode acquisition with the high-frame-rate RF sequence.

Electromechanical wave imaging

Electromechanical wave imaging was performed at a high frame rate of 2000 fps at a 20-cm depth in the standard transthoracic echocardiographic views by emitting circular waves with a virtual source located 10.2 mm behind the 2.5-MHz phased array probe (Fig. 1 i). This flash EWI sequence, relying on unfocused diverging waves, was acquired within a single heartbeat, and the entire field of view was covered at each transmit (Provost et al. 2011b). RF data were acquired for 2 s on six of the seven healthy volunteers twice successively, while longer 6-s acquisitions were performed on the remaining volunteer four successive times. EWI uses dynamic focusing in receive: the RF signal at each pixel is reconstructed by performing a standard sum and delay algorithm in post-processing. The latter consists of using the delayed channel data from each element of the probe and summing all the resulting RF signals (Grondin et al. 2015). The reconstructed RF frames had an angular sampling of 0.7° (i.e., 128 lines over a 90° field of view) and an axial sampling frequency of 20 MHz. After beamforming of the radiofrequency signals on a Tesla GPU (NVIDIA) for faster computation speed, motion estimation (Fig. 1 iib) was performed using a 1-D axial RF cross-correlation algorithm (Luo and Konofagou 2010) with a window size of 10 wavelengths (6.2 mm) and 90% overlap (window shift of 0.62 mm). Then, the axial incremental strains were estimated using a least-squares estimator (Kallel and Ophir 1997) with a kernel of 5 mm. The unfocused EWI transmit sequence was followed by a standard 64-line anatomic B-mode acquisition of 1.5 s at 30 fps and 20-cm depth. The myocardium was manually segmented on the first systolic frame of this anatomic B-mode, selected based on the ECG, and automatically tracked in all subsequent frames through one entire heart cycle using the previously estimated

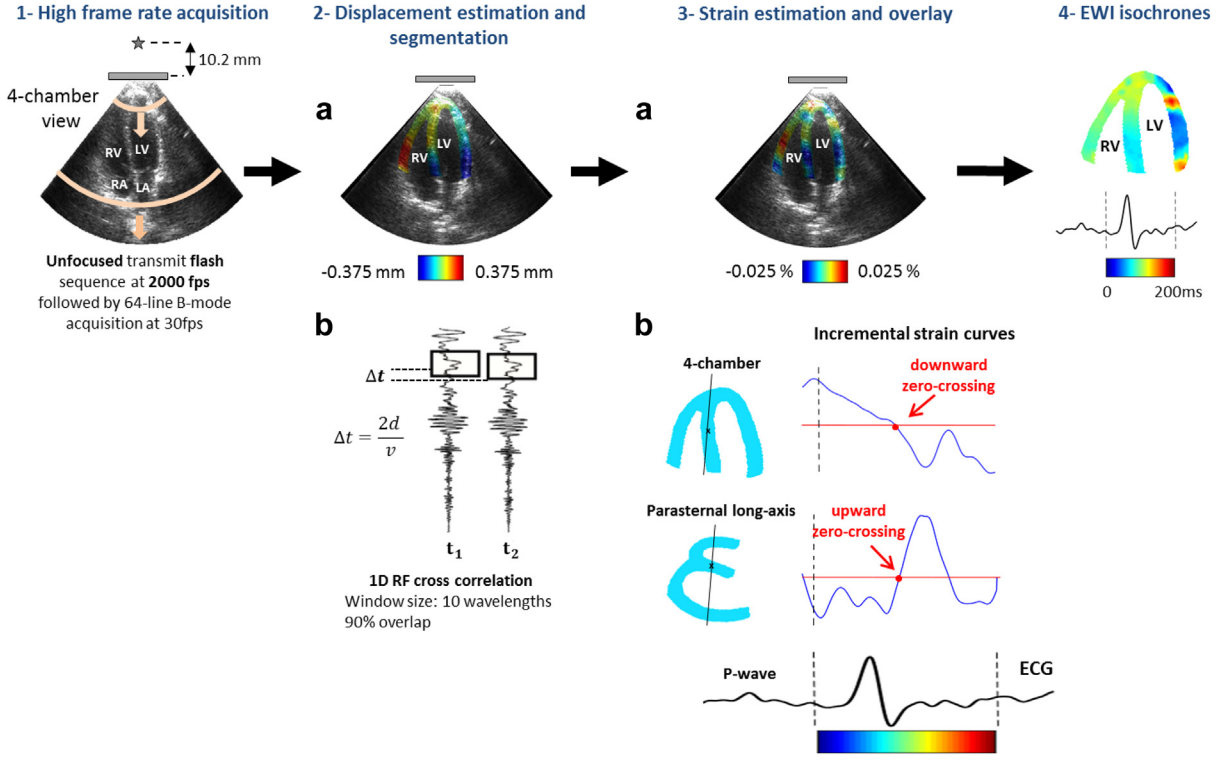

Fig. 1. Complete electromechanical wave imaging (EWI) processing flowchart. (i) Radiofrequency (RF) unfocused circular transmit sequence at a high frame rate (2000 fps) of a standard apical four-chamber view. (ii) Displacement map (a) obtained by applying a 1-D axial RF cross-correlation algorithm (b) with a window size of 10 wavelengths and a 90% overlap. (iii) Axial incremental strains estimated with a least-squares estimator (kernel size: 5 mm) are overlaid on the anatomic B-mode (a) to create the axial incremental strain map. The incremental strain curves (b) for 100 points in the myocardium mask are used to select the first local zero-crossing (intersection with the red horizontal line) after the onset of the P-wave for the atria, respectively, the onset of the QRS complex for the ventricles. (iv) Resulting 2-D four-chamber view activation map from a healthy subject in normal sinus rhythm (NSR). The earliest activation time (0 ms) is represented in *blue*, and the latest (270 ms), in *red*. RV = right ventricle; LV = left ventricle; RA = right atrium; LA = left atrium; ECG = electrocardiogram.

displacements (Luo and Konofagou 2008). The incremental axial displacement maps (Fig. 1 iia) and corresponding incremental axial strain maps (Fig. 1 iiia) were thus easily generated by overlaying the estimated motion and strains in the segmented myocardium contour on the anatomic B-mode image, respectively.

The wavefront of the electromechanical activation was defined as the time point at which the incremental strain value changes from relaxation to contraction after the onset of the QRS complex (Provost et al. 2010). In fact, during active contraction, a change from lengthening to shortening in the axial direction was detected. Therefore, to generate the EWI isochrones or activation time maps (Fig. 1 iv), the local zero-crossing time points of the incremental strain curves need to be mapped. In the apical views, this corresponds to a positive-to-negative zero crossing; this corresponds to a negative-to-positive zero crossing for the parasternal long-axis view as the myocardium walls are not axially aligned with the ultrasound beam in that case (Fig. 1 iiib). The onset of the QRS complex was chosen manually on the ECG and defined by selecting the first downward inflection occurring on the ECG trace after the p-wave. This time point was considered as our activation time origin for the isochrones: $t = 0$ ms (*black dotted line* in Fig. 1 iiib corresponding to the *dark blue* on the activation maps).

For computational efficiency of the isochrone generation, only a subset of points was randomly and automatically selected in MATLAB by downsampling the total number of pixels contained in the myocardium mask. The corresponding zero crossings (ZCs) were manually selected on the incremental strain curves. Regions with noisy strain curves where the locations of the zero-crossing (ZC) could not be determined without ambiguity were discarded and other points were selected. This occurred for about 10% of the total number of points in the subset and included no apparent ZC, multiple successive ZCs of low amplitude and "flat" ZC, where the slope of the strain curve was equal to zero for more than 10 ms. Finally, to obtain smooth and complete EWI isochrones over the entire myocardium mask grid, we applied a Delaunay triangulation-based cubic interpolation to the 2-D scattered ZC timing values. This was performed with the "griddata" function in MATLAB. The cubic interpolation method was applied, as it has been reported to yield uniform activation maps (Costet et al. 2014; Provost et al. 2010). The complete EWI pipeline with its consecutive processing steps can be found in the flowchart in Figure 1. All processing was performed in MATLAB and using the parallel processing toolbox.

Reproducibility

Activation maps of the seven male human subjects in normal sinus rhythm were generated for the three different echocardiographic views. Two successive acquisitions were processed for each of the three views, and two consecutive cardiac cycles were considered per acquisition for all seven healthy volunteers (84 maps = 7 subjects × 2 cycles × 3 views × 2 acquisitions). Eight of the 84 activation maps could not be generated because of a lack of data for the consecutive cardiac cycles, resulting in a total of 76 maps (Table 1). This occurs when the 2-s ECG does not contain two full heart cycles, but rather the end of one cycle, a full second cycle and the beginning of a third cycle. Subsequently, to address these shortcomings, at least five full consecutive heart cycles per acquisition, we acquired longer sequences (6 s) on one of the seven volunteers four successive times in each view. This allowed us to evaluate the reproducibility of our activation maps on a larger amount of measurements with two additional acquisitions per view and three additional consecutive heartbeats per acquisition (48 maps = [2 extra cycles × 3 views × 2 acquisitions] + [5 cycles × 3 views ×2 extra acquisitions]). Figure 2 illustrates the protocol for the different data sets acquired. The *cells in bold font* correspond to the standard protocol for all healthy subjects, whereas the *dotted lines* and *cells in regular font* represent the extra data obtained for the seventh volunteer.

To quantify the repeatability and angle independence of EWI activation maps in human hearts, three different approaches were used to compare the isochrones generated.

Comparison within the same acquisition across consecutive cardiac cycles. Because the mask resulting from the myocardium segmentation was the same for the two consecutive heart cycle maps in a given acquisition, we were able to compute the absolute activation time difference between the isochrones by comparing both

Table 1. 2-D correlation coefficients between the isochrone activation maps of the two consecutive heart cycles (N = 7)

			Four-chamber view		Two-chamber view	
Subject	PLAX 1	PLAX 2	1	2	1	2
1	0.9982	N/A*	0.9945	N/A	0.9990	N/A
2	N/A	0.9932	0.9916	0.9923	0.9878	0.9886
3	0.9933	0.9918	0.9813	0.9896	0.9871	0.9971
4	0.9952	0.9985	0.9811	0.9989	0.9922	0.9753
5	N/A	N/A	N/A	0.9906	0.9974	N/A
6	0.9851	0.9681	0.9861	0.9840	0.9742	0.9795
7	0.9876	0.9854	0.9908	0.9960	0.9963	0.9877

* N/A refers to the eight cases for which the data from the second cardiac cycle were not available for the point-by-point absolute time difference comparison. This occurs when the electrocardiogram recorded simultaneously with the 2-s electromechanical wave imaging acquisition does not contain two full heart cycles, but rather the end of one cycle, a full one and the beginning of a third one.

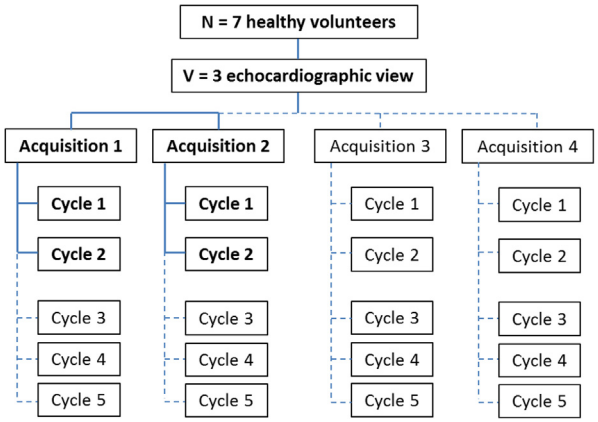

Fig. 2. Acquisition protocol diagram for the three standard echocardiographic views (parasternal long-axis, apical four- and two-chamber). The cells in *boldface type* correspond to the common protocol for all seven healthy subjects (two successive acquisitions with two consecutive heart cycles each), whereas the *dotted lines* and *normal font* cells represent the additional datasets obtained for the seventh subject (two additional acquisitions with five consecutive heart cycles, as well as 3 supplementary beats for the first 2 acquisitions).

maps pixel by pixel. Difference maps were generated, and the resulting activation time difference histograms were plotted (Fig. 3). Our group has already developed and applied this approach to illustrate EWI repeatability across consecutive cardiac cycles during both sinus rhythm and paced open-chest dogs (Costet et al. 2014). Two-dimensional correlation coefficients were also computed between the consecutive heart cycle isochrones to quantify their similarity.

In comparison of isochrones between consecutive acquisitions, a pixelwise comparison is not possible because of similar yet different segmentation. In fact, the isochrone masks varied slightly between acquisitions as the consecutive acquisitions were not entirely identical. Therefore, to assess the reproducibility, isochrone activation time values were averaged in the septal, posterior, lateral and anterior walls of the LV for each view and subsequently compared across the two consecutive acquisitions. We manually segmented the regions of interest on the B-mode (Fig. 4): septal and posterior walls were selected for the parasternal long-axis, septal and lateral walls were considered for the four-chamber and, finally, posterior and anterior walls were examined for the two-chamber view. We then subdivided each LV wall into up to three segments: apical, mid- and basal (Fig. 4, bottom row).

Comparison within equivalent LV wall segments across different imaging views. When different views were compared, an approach similar to that for comparison between consecutive acquisitions was used. Indeed, to quantify the angle independence of EWI, we compared the LV activation time averages in the mid- and basal posterior wall segments between the parasternal and apical two-chamber views and in the basal septal wall segment between the parasternal and apical four-chamber views (Fig. 4).

RESULTS

Reproducibility within same acquisition

Figure 3 illustrates the EWI isochrones maps during normal sinus rhythm for one of the seven healthy volunteers (subject 1) within the same acquisition across consecutive heart cycles. The origin of the isochrones corresponds to the onset of the QRS complex of each cardiac cycle, and we always consider an activation period of 200 ms after that. The regions of earliest activation are represented in blue, while the latest are displayed in red. The top row corresponds to the parasternal long-axis view, and the bottom two rows, the apical four-chamber and two-chamber views, respectively.

Qualitatively, the activation patterns on the isochrones were deemed very similar for the three standard views (Fig. 3a, d, g). In fact, the difference maps appearing mainly in *dark blue* exhibit very few disparities ($<$10 ms) between the isochrones (Fig. 3b, e, h), except in some localized regions displayed in *orange/red*, which present more important differences in activation time ($>$40 ms). These regions are located at the mid-level on the anterior wall of the two-chamber view and near the base and apex on the lateral wall of the four-chamber view. More quantitatively, in the parasternal long-axis view, 80% of the myocardium exhibits activation time differences between two consecutive isochrones of $<$5 ms, which corresponds to 3% of the maximum activation time (Fig. 3c), compared with 90% in the two-chamber view (Fig. 3i). In the apical four-chamber view, 50% of the activation time differences fall under 5 ms and 80% are under 10 ms (Fig. 3f).

Table 1 summarizes the repeatability results across cardiac cycles obtained in all seven subjects. The values listed correspond to the 2-D correlation coefficients between the two consecutive activation maps. Less satisfying repeatability performance was observed for subject 6 in the parasternal long-axis view, with the lowest correlation coefficient at 0.9681. On the other hand, our best reproducibility case corresponds to the apical two-chamber view for subject 1, with a high correlation value of 0.999. Finally, the average 2-D correlation coefficient between the two consecutive cycle isochrones across all volunteers was 0.9893.

More specifically, Figure 5 depicts a heat map of the 2-D correlation coefficients for the four successive acquisitions in each view for subject 7. Because the acquisitions were 6 s long in that case, we were able to generate the activation maps of five consecutive heart cycles, resulting in a total of 10 comparisons per acquisition (cycle i vs.

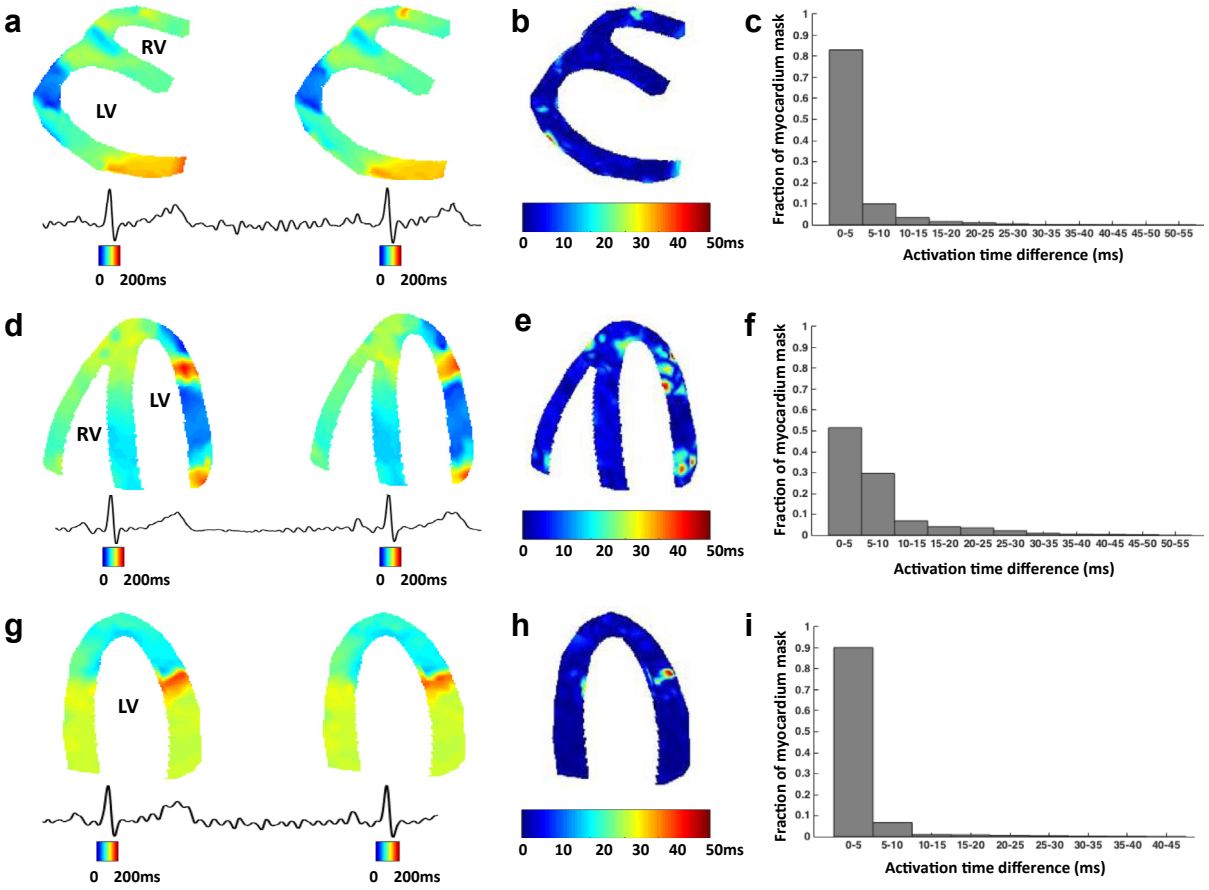

Fig. 3. Electromechanical wave imaging (EWI) reproducibility during sinus rhythm for a healthy subject within the same acquisition across consecutive heart cycles. The origins of the isochrones correspond to the onset of the QRS complex. (a) Parasternal long-axis view isochrones for two consecutive cardiac cycles. (b) Difference map and (c) histogram of the absolute activation time difference between the two parasternal long-axis view isochrones. (d) Apical four-chamber view isochrones for two consecutive cardiac cycles. (e) Difference map and (f) histogram of the absolute activation time difference between the two apical four-chamber isochrones. (g) Apical two-chamber view isochrones for two consecutive cardiac cycles. (h) Difference map and (i) histogram of the absolute activation time difference between the two apical two-chamber isochrones. LV = left ventricle; RV = right ventricle.

cycle j where $i \neq j$ and $\in$ [1:5]). Each square corresponds to a color-coded correlation coefficient from 1 in *dark green* for perfect similarity to 0.95 in *dark red*. Overall, the large majority of squares displayed on the figure are green: only 13 of the 120 comparisons lay below 0.975 (*yellow* to *red* on color bar). The lowest correlation coefficient was 0.9548 in acquisition 1 of the parasternal long-axis view when comparing cycle 1 to cycle 4, whereas the highest was 0.9977 in the third acquisition of the apical four-chamber view when comparing cycles 2 and 3.

Reproducibility within same view

The reproducibility of EWI during sinus rhythm within the same view across successive acquisitions is depicted in Figure 6 for the same healthy subject as in Figure 3. The isochrones for the first acquisition of each view (parasternal long-axis [a], four-chamber [c] and two-chamber [e]) and for the second acquisition of these same views (b, d and f) are provided. The origin of the isochrones corresponds to the onset of the QRS complex, and the color bar spans from 0 to 200 ms. Comparison across acquisitions in the same view yielded very similar results in terms of the EW propagation pattern (Fig. 6a vs. 6b, Fig. 6d vs. 6e, Fig. 6g vs. 6h). Regardless of the view, the earliest and latest activated regions remain at the same regions from one acquisition to the other.

In addition, the boxplots in the right column of Figure 6 illustrate the activation time distribution in the left ventricle walls through two successive acquisitions for each standard view: (c) posterior and septal walls in parasternal long-axis, (f) lateral and septal walls in apical four-chamber and (i) posterior and anterior walls in apical two-chamber views. The colors are consistent with the regions of interest (ROI) selected in Figure 4: the *cyan*

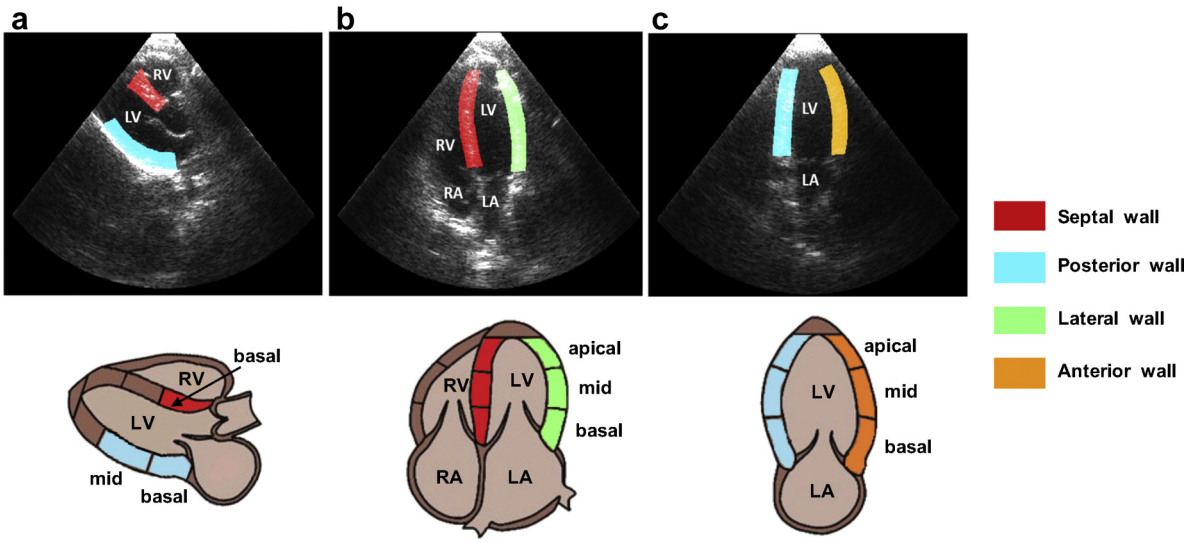

Fig. 4. Standard electromechanical wave imaging (EWI) echocardiographic imaging views. (a) Parasternal long-axis view. (b) Apical four-chamber view. (c) Apical two-chamber view. The left ventricle walls (excluding the apex) were segmented manually, and the colored regions of interest are overlaid on the gray-scale B-mode. The septal wall is visible in red, the posterior wall in *cyan*, the lateral wall in *green* and the anterior wall in *orange*. In the bottom row is a schematic of each view with the subdivision of the LV walls into segments. RV = right ventricle; LV = left ventricle; RA = right atrium; LA = left atrium.

boxes correspond to the posterior wall, the *red boxes* to the septal wall, the *green boxes* to the lateral wall and the *orange boxes* to the anterior wall. Lastly, the *black dots* represent the means of the distributions, and the *horizontal colored lines* in the boxes are the medians. The two *vertical dotted segments* extending from the top and bottom of the boxes are called "whiskers." The latter are displayed to indicate the variability outside the upper and lower quartiles of the data sets. It should be noted that for all boxplots in this article, the whisker extremities were defined as the highest/lowest values included within three times the interquartile range (IQR) of the box edges, contrary to the usual standard 1.5 * IQR value.

Qualitatively, the spread of activation times in each wall was found to be comparable between acquisitions for all cases; the interquartile ranges represented by the box spans are overall identical. More specifically, we focused on the means of the distribution in each LV wall segment as our final comparison metric (Table 2, subject 1). Nevertheless, for the sake of visibility on the boxplot, entire walls were considered before subdivision into segments (Fig. 4, top row). Average activation times in the parasternal long-axis view (Fig. 6c) varied by 0.44% in the septal wall (93.6–94.3 ms) to 0.14%, in the posterior wall (108–108.2 ms). In the apical two-chamber view (Fig. 6i), the anterior wall average activation times differed from each other by 2.02% (100.2–103.7 ms), and the posterior wall average activation times varied by 1.5% (99.7– 102.3 ms). Finally, in the four-chamber view (Fig. 6f), the highest average activation time fluctuation of 4.27% is noted in the lateral wall (79.2–86.6 ms), with the smallest variation of 0.02% for the septal wall (89.43–89.47 ms).

A summary of the reproducibility results obtained for all seven volunteers across two successive acquisitions in the same imaging views can be found in Table 2. We always performed the comparison between the first cardiac cycles processed for each acquisition. The variation in average activation times within the smaller LV wall segments (Fig. 4, bottom row) across the two consecutive acquisitions are listed as percentages. The latter are calculated as the percentage deviation with respect to the latest activation time displayed in the two successive acquisitions, in milliseconds. Variation ranges from 0.02% in the basal anterior wall segment in the apical two-chamber view for subject 5 to 25.31% in the basal posterior wall segment in the apical two-chamber view for subject 2. Although 8 of the 105 values exceed 15%, the average variation value satisfyingly lies at 6.19%.

Angle independence

In Figure 7 is a Bland–Altman plot of the LV wall activation time averages for the seven healthy subjects. The plot illustrates EWI reproducibility during sinus rhythm for all volunteers within equivalent LV wall segments across different imaging views. The seven different colors correspond to the seven different volunteers. The two consecutive acquisitions were averaged for each of the three standard echocardiographic views, and each subject is represented by three points. The first point is the comparison of activation time measurements in the basal septal wall between the parasternal

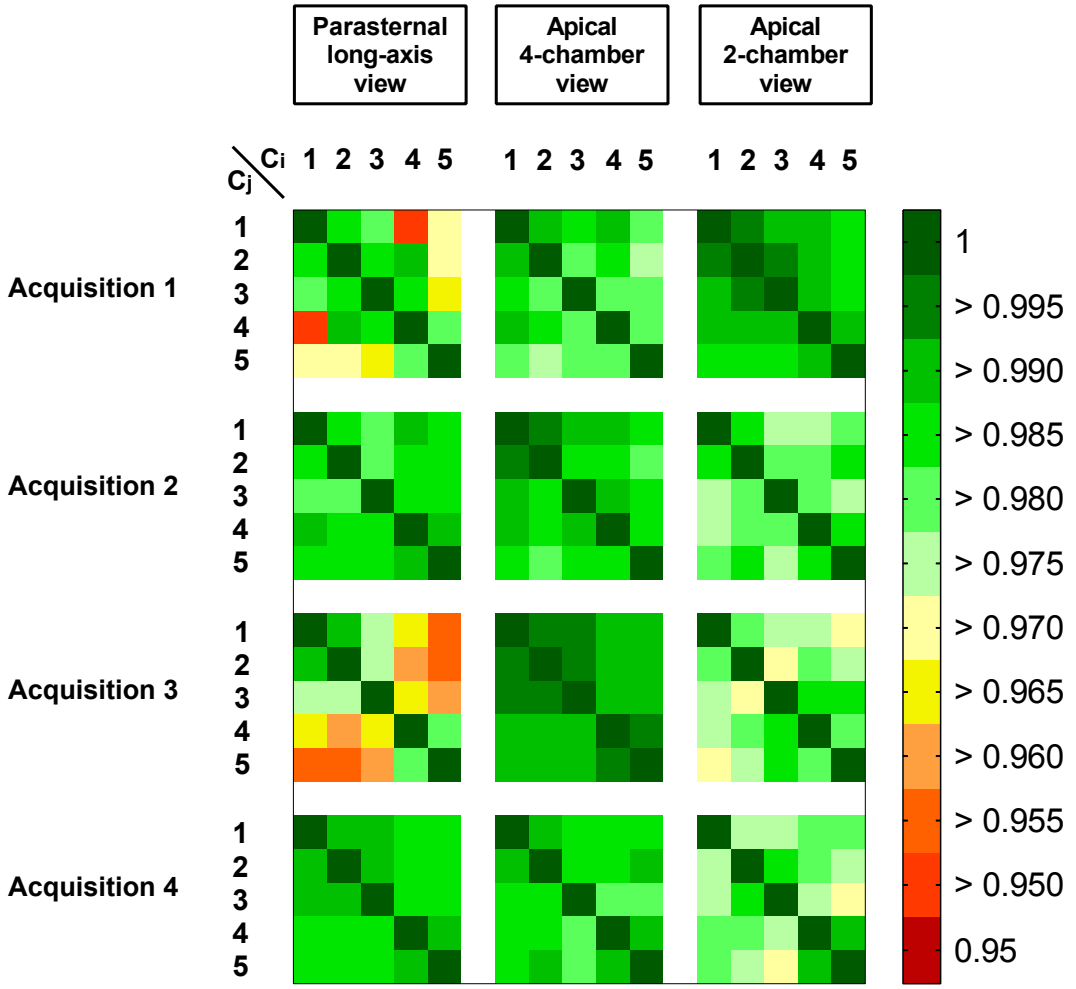

Fig. 5. Heat map of the 2-D correlation coefficients between consecutive cardiac cycle activation maps for subject 7 in three different views (parasternal long-axis, apical four- and two-chamber) with four successive acquisitions each. Five consecutive heartbeats were studied, resulting in a total of 10 comparisons per acquisition (cycle i C_i vs. cycle j C_j where $i \neq j$ and both $\in$ [1:5]). The 12 squares each represent one acquisition. Each small cell within the 5×5 squares corresponds to a color-coded correlation coefficient; the highest similarity values are represented in *green*, and the lowest, *in red*.

long-axis and apical four-chamber views, whereas the second and third points represent the comparison of the basal and mid-posterior wall, respectively, between the parasternal long-axis and apical two-chamber views. The x-axis displays the mean LV wall segment activation time averages for both methods, whereas the y-axis is the difference between the two values in milliseconds.

All measurements were within the limits of agreement or 95% confidence interval defined by the mean $\pm$ 1.96 times the standard deviation, and the bias found was 3.2 ms. The latter was computed from the Bland-Altman plot as the mean activation time average difference between the two views among the seven healthy volunteers. The standard deviation of the mean values, also called coefficient of variation was 12%. These results indicate that EWI and its subsequent generation of LV wall activation time averages can be used reliably to characterize the activation sequence of healthy subjects in normal sinus rhythm independently of the imaging view.

DISCUSSION

Electromechanical wave imaging is an ultrasound-based imaging technique that can non-invasively map the electromechanical activity in all four heart chambers *in vivo* at very high spatial and temporal resolution. At the tissue level, the depolarization of the cardiomyocytes triggers the electromechanical activation, corresponding to the first time at which the cardiac muscle transitions from a relaxation to a contraction state. Spatially, this electromechanical activation forms the EW front that follows the propagation pattern of the electrical activation sequence.

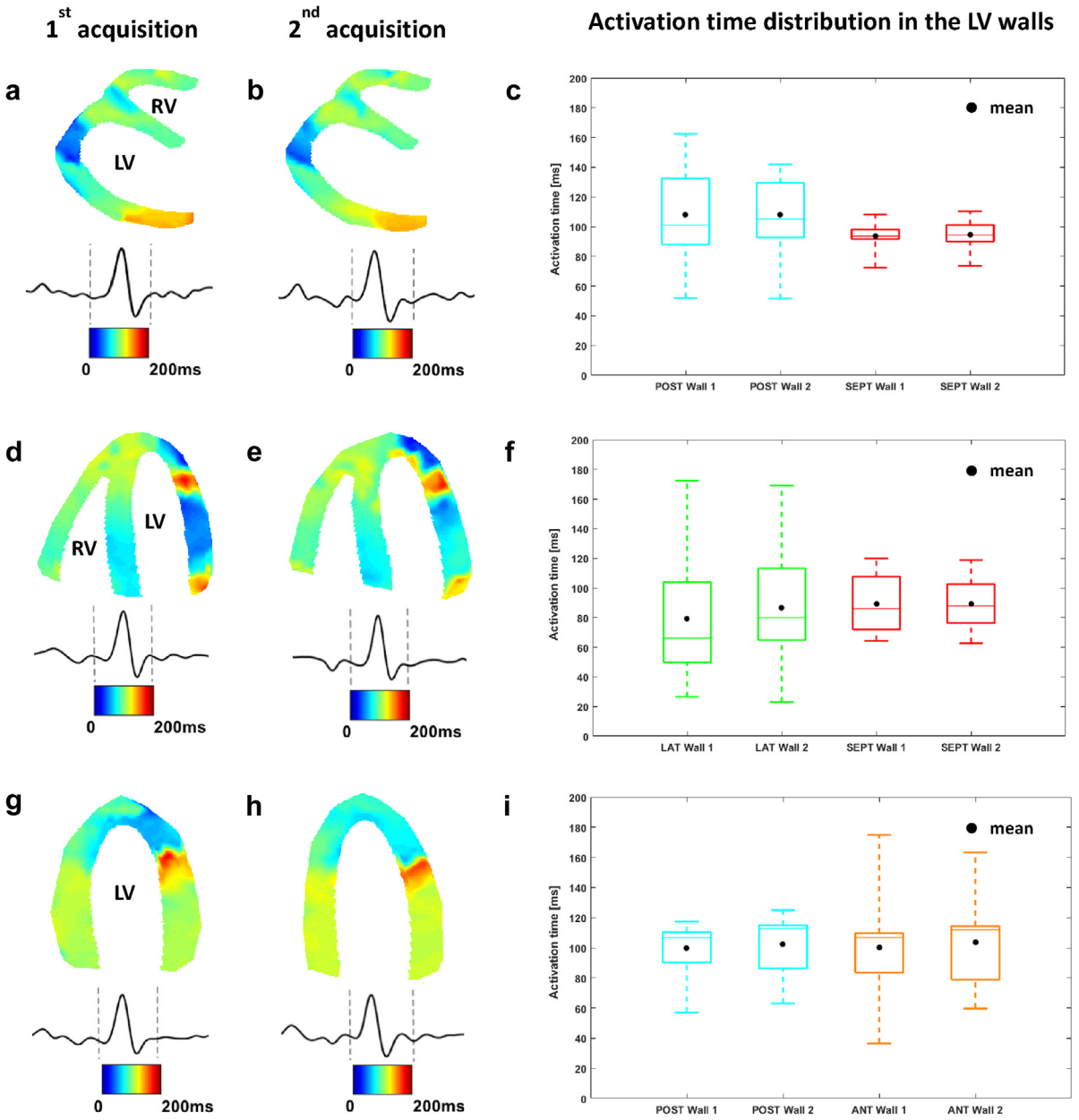

Fig. 6. Electromechanical wave imaging (EWI) reproducibility during sinus rhythm for a healthy subject within the same view across two successive acquisitions. The origin of the isochrones corresponds to the onset of the QRS complex. (a) Parasternal long-axis view isochrone for the first acquisition. (b) Parasternal long-axis view isochrone for the second acquisition. (c) Apical four-chamber view isochrone for the first acquisition. (d) Apical four-chamber view isochrone for the second acquisition. (e) Apical two-chamber view isochrone for the first acquisition. (f) Apical two-chamber view isochrone for the second acquisition. The boxplots display the activation time distribution in the left ventricle walls through two successive acquisitions for each standard view: (c) parasternal long-axis view, (f) apical four-chamber view and (i) apical two-chamber view. The colors on the plots are consistent with the regions of interest selected on Figure 2: the *cyan* boxes represent the posterior wall (POST), the *red* boxes correspond to the septal wall (SEPT), the *green boxes* to the lateral wall (LAT) and the *orange boxes* to the anterior wall (ANT). The tops of the boxes mark the 75th percentile of the data sets; the bottom corresponds to the 25th percentile. LV = left ventricle; RV = right ventricle.

In this study, we used EWI to transthoracically image healthy human hearts in normal sinus rhythm. The objectives of this study were to determine the reproducibility and angle independence of our method for the assessment of electromechanical activation in normal human subjects *in vivo*.

In Figure 3, we established EWI repeatability within a single heart for a given acquisition across consecutive

Table 2. Variation in average activation times within left ventricle wall segments across two consecutive acquisitions in the three imaging views (N = 7)*

Parasternal long-axis view			
Subject	Basal posterior	Mid-posterior	Basal septum
1	2.20%	3.30%	0.44%
2	2.91%	1.69%	1.15%
3	2.12%	7.23%	2.53%
4	12.07%	7.39%	4.22%
5	11.53%	1.57%	5.01%
6	1.48%	0.99%	1.37%
7	6.07%	6.56%	9.28%

Four-chamber apical view						
Subject	Basal lateral	Mid-lateral	Apical lateral	Basal septum	Mid-septum	Apical septum
1	4.58%	10.49%	3.95%	1.06%	2.19%	3.51%
2	4.47%	18.74%	2.76%	17.97%	14.67%	5.76%
3	19.68%	6.35%	5.85%	9.42%	3.34%	13.90%
4	1.98%	3.77%	0.05%	7.94%	2.66%	1.51%
5	4.34%	3.12%	3.88%	1.04%	4.87%	4.71%
6	2.84%	5.71%	2.41%	2.42%	1.02%	10.69%
7	12.89%	10.40%	7.67%	23.24%	1.94%	2.63%

Two-chamber apical view						
Subject	Basal posterior	Mid-posterior	Apical posterior	Basal anterior	Mid-anterior	Apical anterior
1	3.11%	1.92%	0.10%	2.81%	2.09%	5.92%
2	25.31%	10.10%	5.87%	1.78%	14.20%	0.51%
3	15.16%	19.72%	6.14%	7.01%	2.84%	1.17%
4	7.62%	8.66%	0.44%	12.34%	6.51%	8.35%
5	1.04%	1.18%	1.75%	0.02%	0.36%	0.77%
6	8.99%	10.46%	8.57%	2.96%	10.83%	21.52%
7	13.47%	6.54%	4.29%	6.15%	13.54%	3.95%

* We always performed the comparison between the first cardiac cycles processed for each acquisition.

cardiac cycles during NSR in humans for the three different echocardiographic standard views by performing a point-by-point comparison of the isochrone maps. These results confirm previous findings by our group that EWI was repeatable within the same acquisitions across consecutive cardiac cycles in open-chest dogs (Costet et al. 2014). Those results also indicate that despite the loss in resolution in transthoracic human echocardiography caused by the additional layers the ultrasound waves have to go through, the reproducibility of our technique is confirmed. According to the difference maps and the histograms of the difference in activation time, more than 80% of the pixels have a difference in activation time <5 ms, for both the apical two-chamber and parasternal long-axis views (Fig. 3c, i). In the apical four-chamber view, 50% of the myocardium has a difference <5 ms, and 80% has a difference <10 ms (Fig. 3f). However, the discrepancies displayed in *orange/red* on the four-chamber difference map are very sparse (Fig. 3e). These regions are restricted to "high activation time gradient" locations on the lateral wall in the consecutive isochrones. In fact, the few difference areas appear close to discontinuities and not in the center of a homogeneous pattern such as the lateral midwall (Fig. 3d). The high gradient term refers to the sudden jumps in activation times on the isochrones, for instance, near the apex mid-basally and close to the left atria junction. Because the electromechanical activation is a wave, it is assumed to propagate continuously. Thus, we would expect smooth transitions in the activation time gradient on the maps.

Discontinuities in the pattern of activation may be explained by the fact that, albeit standard, only 2-D slices were acquired while the EW is a 3-D propagation phenomenon. Thus, disruption in the gradient might result from out-of-plane motion. In addition, this could also occur because when generating the isochrones, the points considered in the myocardium are randomly chosen and not all are taken into account before interpolation, as indicated previously. Thus, a higher point density in the late activated region compared with fewer points in the surrounding early activated region could affect the interpolation step and result in disparities in the isochrone patterns. This issue could be overcome by automating the processing pipeline and examining every single pixel contained in the mask, without requiring manual zero-crossing selection. Our group is currently investigating the

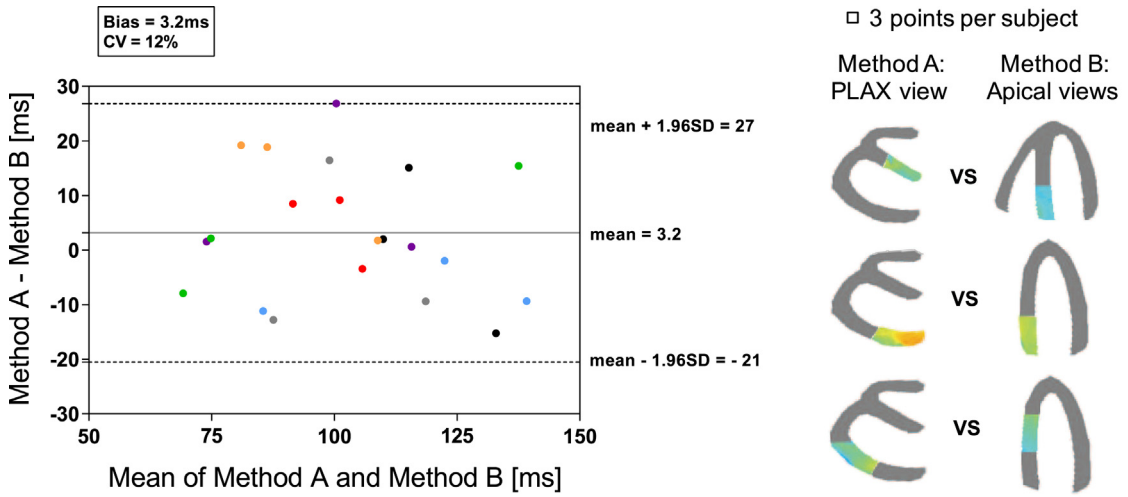

Fig. 7. Bland–Altman plot of LV wall activation time averages for the seven healthy subjects. The plot illustrates electromechanical wave imaging (EWI) reproducibility during SR for seven healthy volunteers within equivalent LV wall segments across different imaging views. The seven different colors correspond to the seven different subjects. The two consecutive acquisitions were averaged for each of the three views, and each subject is represented by three points. The first point corresponds to the comparison of the basal septal wall between the parasternal long-axis and apical four-chamber views; the second and third points represent the comparison of the basal, respectively, mid-posterior wall between the parasternal long-axis and apical two-chamber views. CV = coefficient of variation (standard deviation of the mean values in %); PLAX = parasternal long-axis view; LV = left ventricle.

implementation of a new processing algorithm for automated isochrone generation. This algorithm considers all points in the mask, automatically selects the zero crossings according to a list of conditions that ZCs should satisfy and eliminates the uncertain points. "Clear" ZCs would be defined based on the amplitude of the crossing peak, the steepness of the strain curve slope at the crossing and the number of multiple successive ZCs (Bunting et al. 2017).

In Table 1, we further investigated EWI reproducibility across consecutive cardiac cycles for the seven healthy volunteers using the 2-D correlation coefficient as our similarity metric. More than three-quarters of the correlation coefficients listed in the table were satisfyingly above 0.985. Furthermore, the heat map of the 2-D correlation coefficients for subject 7 (Fig. 5) revealed that even when we increased the number of comparisons to five consecutive heart beats and four successive acquisitions, we were still able to obtain reproducible results with an average correlation of 0.9844. In addition, we observed that all the coefficients <0.970 appear only in the comparisons resulting from the parasternal long-axis view acquisitions. This may be due to the higher uncertainty in the zero-crossing selection, as the orientation of the LV walls with respect to the ultrasound beam direction is not always the same in this view. This alignment variation is further explained below under Limitations.

In Figure 6, we also assessed EWI activation timing reproducibility between separate acquisitions of the same view during NSR for subject 1. The general EW propagation pattern displayed on the activation maps was unchanged from one acquisition to the next. In the apical four-chamber view, the highest activation time average fluctuation was obtained in the lateral wall, reaching 4.27%, with a small variation of 0.02% for the septal wall. Global average activation times in parasternal long-axis and two-chamber view walls varied only by 0.29% and 1.76%, respectively. As for the activation time average variation in the smaller LV wall segments (Table 2), the mean across all seven subjects was 6.19%, with more than three-quarters of the average values lying below a 10% disparity between successive acquisitions.

Finally, we found that we were able to achieve similar activation times across different views in the same cardiac regions of the isochrones. As seen on the Bland–Altman plot in Figure 7, LV wall segment activation time averages were fairly consistent within the same subject across the different standard echocardiographic imaging views. Indeed, all the measurement points were within the limits of agreement. The largest activation time average difference across views was observed for subject 3 with a value of 26.8 ms. This is still low compared with known characteristic variations within a single conduction disorder patient. In fact, typical values for transseptal conduction times are in general larger than 40 ms in patients with left bundle branch block (Prinzen and Auricchio 2008). These findings confirm the angle independence of EWI for the assessment of electromechanical activation *in vivo* as previously established *in silico* (Provost et al. 2011c).

There are several limitations to this study. A limitation arises from the orientation of the LV walls with respect to the ultrasound beam direction. In fact, EWI relies on a 1-D RF cross-correlation, and the strains are estimated axially. For the apical four- and two-chamber views, selection of the correct zero crossings is quite straightforward. Because the walls are axially aligned with the ultrasound beam on the B-mode (Fig. 4b, c), the first positive to negative zero crossing after the onset of the QRS complex was selected. However, for the parasternal long-axis view, these may not constitute the optimal criteria. The LV walls are not always parallel to the bottom and top borders of the B-mode image (Fig. 4a); they are slightly angled, neither completely perpendicular to the ultrasound beam nor axially aligned. Thus, negative and positive slopes were considered. Identifying the most suitable orientation transition is challenging. This limitation could be mitigated by implementing an automated technique of discriminating between the two types of zero crossings. Systematically computing the angle between the orientation of the wall and the direction of the ultrasound beam could be a good alternative in determining whether we should expect thickening or thinning of the wall for a given point. Such computer vision techniques already exist for automated and robust Doppler angle estimation between the insonifying ultrasound beam and the vessel walls (Pan et al. 2000; Saad et al. 2009). The latter rely on least-squares line-fitting algorithms of the segmented vessel and could be adapted to the assessment of the myocardium wall orientation by fitting a higher-order polynomial or spline. This additional feature will be implemented into the automated isochrone processing pipeline.

Another main limitation lies in the fact that it is challenging to quantitatively compare the electromechanical activation patterns across different acquisitions and imaging views without averaging the activation times, as the segmentation was not precisely the same and the walls cannot be registered perfectly. For a more accurate comparison and better quantification of the reproducibility, we should consider acquiring data with a 2-D matrix array. Three-dimensional echocardiography in a single cardiac cycle would require additional hardware and processing methods, but has been found to be feasible using plane waves (Papadacci et al. 2017a) or diverging waves for a wider field of view. Our group recently reported the initial feasibility of 3-D strain imaging in the heart at very high volume rates (Papadacci et al. 2017b). Further optimization will be conducted to perform 3-D electromechanical wave imaging.

Finally, EWI was recently validated in canine hearts against two clinically available mapping techniques. Electromechanical activation patterns were compared with electrical results obtained from a 64-electrode basket catheter inserted into the LV, during sinus rhythm, as well as under epicardial and endocardial pacing (Grondin et al. 2016). EWI was also validated both epicardially and endocardially in all four chambers of the heart under normal sinus rhythm and epicardial LV pacing with conventional 3-D electroanatomic mapping using a St. Jude's EnSite system (Costet et al. 2016). Electromechanical activation times were found to be highly correlated with the electrical activation times obtained from both electroanatomic mapping techniques in canines.

Electromechanical wave imaging is currently being studied as a potential tool to assist clinicians in identifying arrhythmogenic zones and guide ablation procedures. An ongoing clinical study deals with arrhythmia patients undergoing electrophysiological studies and RF ablation. Combination of EWI with myocardial elastography (Bunting et al. 2016; Grondin et al. 2015; Papadacci et al. 2017a, 2017b) and their complementarities is also a topic of ongoing studies. In conjunction with the catheter-based electroanatomic mapping frequently used in the clinic, EWI could non-invasively help physicians for the early detection, diagnosis, treatment planning, monitoring and follow-up of patients with arrhythmia through ultrasound-based mapping of their electromechanical activation sequence. In addition, EWI could easily be integrated into existing echocardiography systems and, therefore, diagnostic protocol and assessment clinical routine, at no or minimal additional cost.

CONCLUSIONS

Electromechanical wave imaging was hereby illustrated to be capable of transthoracically characterizing the sinus rhythm electromechanical activation and of reliably obtaining similar activation time averages in the LV wall segments between different echocardiographic acquisitions and views. These findings indicate that EWI can non-invasively map the electromechanical activation in sinus rhythm in human hearts *in vivo* and result in reproducible and angle-independent activation maps (i) across consecutive heart cycles; (ii) across separate acquisitions; and (iii) across different views.

Acknowledgments—This study was supported in part by the National Institutes of Health (R01 EB006042 and R01 HL114358).—The authors express their very great appreciation to Koki Nakanishi, MD. for his time and valuable assistance acquiring the data. The authors also thank Shunichi Homma, MD, for his contribution to this article, and Ethan Bunting, Julien Grondin, PhD., Vincent Sayseng, and Pierre Nauleau, PhD, in the same group for helpful discussions.

REFERENCES

Bers DM. Cardiac excitation–contraction coupling. Nature 2002;415:198–205.

Bunting E, Papadacci C, Wan E, Grondin J, Konofagou EE. Intracardiac myocardial elastography for lesion quantification in cardiac

radiofrequency ablation. IEEE Int Ultrason Symp Proc 2016;1–4. http://dx.doi.org/10.1109/ULTSYM.2016.7728575.
Bunting E, Lambrakos L, Kemper P, Whang W, Garan H, Konofagou EE. Imaging the propagation of the electromechanical wave in heart failure patients with cardiac resynchronization therapy. Pacing Clin Electrophysiol 2017;40:35–45.
Cordeiro JM, Greene L, Heilmann C, Antzelevitch D, Antzelevitch C. Transmural heterogeneity of calcium activity and mechanical function in the canine left ventricle. Am J Physiol Heart Circ Physiol 2004;286:H1471–H1479.
Costet A. Electromechanical wave imaging for the in vivo characterization and assessment of cardiac arrhythmias. Doctoral dissertation. Columbia University Academic Commons; 2016.
Costet A, Provost J, Gambhir A, Bobkov Y, Danilo P Jr, Boink GJJ, Rosen MR, Konofagou EE. Electromechanical wave imaging of biologically and electrically paced canine hearts in vivo. Ultrasound Med Biol 2014;40:177–187.
Costet A, Wan E, Bunting E, Grondin J, Garan H, Konofagou EE. Electromechanical wave imaging (EWI) validation in all four cardiac chambers with 3D electroanatomic mapping in canines in vivo. Phys Med Biol 2016;61:8105–8119.
Costet A, Wan E, Melki L, Bunting E, Grondin J, Garan H, Konofagou EE. Non-invasive characterization of focal arrhythmia with electromechanical wave imaging. IEEE Trans Med Imaging 2017. in review.
Esmaeilzadeh M, Omran MTS, Maleki M, Haghjoo M, Noohi F, Haghighi ZO, Sadeghpour A, Davari PN, Abkenar HB. Noninvasive localization of accessory pathways in patients with Wollf–Parkinson–White syndrome: A strain imaging study. J Tehran Univ Heart Cent 2013;8:65–69.
Glass L, Hunter P, McCulloch A, (eds). Theory of heart: Biomechanics, biophysics, and nonlinear dynamics of cardiac function. Berlin/Heidelberg: Springer-Verlag; 1991.
Grondin J, Wan E, Gambhir A, Garan H, Konofagou EE. Intracardiac myocardial elastography in canines and humans in vivo. IEEE Trans Ultrason Ferroelectr Freq Control 2015;62:337–349.
Grondin J, Costet A, Bunting E, Gambhir A, Garan H, Wan E, Konofagou EE. Validation of electromechanical wave imaging in a canine model during pacing and sinus rhythm. Heart Rhythm 2016;13:2221–2227.
Ishizu T, Seo Y, Igarashi M, Sekiguchi Y, Machino-Ohtsuka T, Ogawa K, Kuroki K, Yamamoto M, Nogami A, Kawakami Y, Aonuma K. Noninvasive localization of accessory pathways in Wolff–Parkinson syndrome by three-dimensional speckle tracking echocardiography. Circ Cardiovasc Imaging 2016;9:e004532.
Kallel F, Ophir J. A least-squares strain estimator for elastography. Ultrason Imaging 1997;19:195–208.
Knackstedt C, Schauerte P, Kirchhof P. Electro-anatomic mapping systems in arrhythmias. Europe 2008;10:iii28–iii34.
Konofagou EE, Luo J, Salena D, Cervantes DO, Coromillas J, Fujikura K. Noninvasive electromechanical wave imaging and conduction-relevant velocity estimation in vivo. Ultrasonics 2010;50:208–215.
Luo J, Konofagou EE. High-frame rate, full-view myocardial elastography with automated contour tracking in murine left ventricles in vivo. IEEE Trans Ultrason Ferroelectr Freq Control 2008;55:240–248.
Luo J, Konofagou EE. A fast normalized cross-correlation calculation method for motion estimation. IEEE Trans Ultrason Ferroelectr Freq Control 2010;57:1347–1357.
Mehra R. Global public health problem of sudden cardiac death. J Electrocardiol 2007;40:S118–S122.
Mozaffarian D, Benjamin EJ, Go AS, Arnett DK, Blaha MJ, Cushman M, Das SR, De Ferranti S, Després JP, Fullerton HJ, Howard VJ, Huffman MD, Isasi CR, Jiménez MC, Judd SE, Kissela BM, Lichtman JH, Lisabeth LD, Liu S, Mackey RH, Magid DJ, McGuire DK, Mohler ER III, Moy CS, Muntner P, Mussolino ME, Nasir K, Neumar RW, Nichol G, Palaniappan L, Pandey DK, Reeves MJ, Rodriguez CJ, Rosamond W, Sorlie PD, Stein J, Towfighi A, Turan TN, Virani SS, Woo D, Yeh RW, Turner MB, Association Statistics Committee; Stroke Statistics Subcommittee. Heart disease and stroke statistics–2016 update: A report from the American Heart Association. Circulation 2016;133:e38–e360.
Packer DL. Evolution of mapping and anatomic imaging of cardiac arrhythmias. J Cardiovasc Electrophysiol 2004;15:839–854.
Pan L, Washburn MJ, Mo LYL. Method and apparatus for automatic Doppler angle estimation in ultrasound imaging. U.S. Patent 6,068,598; issue date: May 30, 2000.
Papadacci C, Bunting E, Konofagou EE. 3D quasi-static elastography with plane wave in vivo. IEEE Trans Med Imaging 2017a;36:357–365.
Papadacci C, Bunting E, Wan E, Nauleau P, Konofagou EE. 3D myocardial elastography in vivo. IEEE Trans Med Imaging 2017b;36:618–627.
Prinzen FW, Auricchio A. Is echocardiographic assessment of dyssynchrony useful to select candidates for cardiac resynchronization therapy? Echocardiography is not useful before cardiac resynchronization therapy if QRS duration is available. Circ Cardiovasc Imaging 2008;1:79–85.
Provost J, Lee WN, Fujikura K, Konofagou EE. Electromechanical wave imaging of normal and ischemic hearts in vivo. IEEE Trans Med Imaging 2010;29:625–635.
Provost J, Lee WN, Fujikura K, Konofagou EE. Imaging the electromechanical activity of the heart in vivo. Proc Natl Acad Sci USA 2011a;108:8565–8570.
Provost J, Nguyen VT, Legrand D, Okrasinski S, Costet A, Gambhir A, Garan H, Konofagou EE. Electromechanical wave imaging for arrhythmias. Phys Med Biol 2011b;56:L1–L11.
Provost J, Gurev V, Trayanova N, Konofagou EE. Mapping of cardiac electrical activation with electromechanical wave imaging: An in silico–in vivo reciprocity study. Heart Rhythm 2011c;8:752–759.
Saad AA, Loupas T, Shapiro LG. Computer vision approach for ultrasound Doppler angle estimation. J Digital Imaging 2009;22:681–688.
Walker WF, Trahey GE. A fundamental limit on delay estimation using partially correlated speckle signals. IEEE Trans Ultrason Ferroelectr Freq Control 1995;42:301–308.
Wang S, Lee WN, Provost J, Luo J, Konofagou EE. A composite high-frame-rate system for clinical cardiovascular imaging. IEEE Trans Ultrason Ferroelectr Freq Control 2008;55:2221–2233.
Zipes DP, Wellens HJJ. Sudden cardiac death. Circulation 1998;98:2334–2351.
Zoni-Berisso M, Lercari F, Carazza T, Domenicucci S. Epidemiology of atrial fibrillation: European perspective. J Clin Epidemiol 2014;6:213–220.